

Fitting Gravitational Lenses: Truth or Delusion

N. Wyn Evans^{1,2} and Hans J. Witt³

¹ *Theoretical Physics, 1 Keble Rd, Oxford, OX1 3NP*
² *Institute of Astronomy, Madingley Rd, Cambridge, CB3 0HA*
³ *Baumkamp 8, 22299 Hamburg, Germany*

2 December 2024

ABSTRACT

The observables in a strong gravitational lens are usually just the image positions and sometimes the flux ratios. We develop a new and simple algorithm which allows a set of models to be fitted exactly to the observations. Taking our cue from the strong body of evidence that early-type galaxies are close to isothermal, we assume that the lens is scale-free with a flat rotation curve. However, our algorithm allows full flexibility as regards the angular structure of the lensing potential. Importantly, all the free parameters enter linearly into the model and so *the lens and flux ratio equations can always be solved by straightforward matrix inversion*. The models are only restricted by the fact that the surface mass density must be positive. The transmission of the errors in the observations to uncertainties in the fitted parameters can be followed exactly and the full covariance matrix can be readily generated.

We use this new algorithm to examine some of the claims made for anomalous flux ratios. It has been argued that such anomalies betray the presence of substantial amounts of substructure in the lensing galaxy. We demonstrate by explicit construction that some of the lens systems for which substructure has been claimed can be well-fit by smooth lens models. This is especially the case when the systematic errors in the flux ratios (caused by microlensing or scatter-broadening or differential extinction) are taken into account. However, there is certainly one system (B1422+231) for which the existing smooth models are definitely inadequate and for which substructure may be implicated. Within a few tens of kpc of the lensing galaxy centre, dynamical friction is very efficient at dissolving any substructure. Very little substructure ($\lesssim 1\%$ of the mass) is projected within the Einstein radius. The numbers of strong lenses for which substructure is currently being claimed are so large that this contradicts rather than supports cold dark matter theories.

Key words: gravitational lensing – galaxies: structure – galaxies: elliptical – dark matter

1 INTRODUCTION

The fitting of models to observational data has always been a major concern in strong gravitational lensing (e.g., Schechter 2000). In most cases, the lens is only composed of 2 (a “doublet”) or 4 (a “quadruplet”) point-like images. For the doublets, the observable constraints are the four relative coordinates of the images with respect to the lensing galaxy, together with the one flux ratio of the first image to the second. For the quadruplets, this becomes eight relative coordinates and three flux ratios. Only for a handful of lens systems are time delays available. It therefore happens very frequently that lens models have more degrees of freedom than the number of constraining observations. In fact, the situation is often even worse than we have just described. Sometimes the centre of the lensing galaxy itself cannot be reliably identified. Sometimes a lens system is complicated

by the possible effects of nearby bright galaxies. Very often, the flux ratios are untrustworthy, either because of differential extinction in the optical bands (e.g., Falco et al. 1999) or because of microlensing in the optical and radio (e.g., Irwin et al. 1989; Koopmans & de Bruyn 2000) or because of scintillation and scatter-broadening in the radio (e.g., Patnaik et al. 1992, Jones et al. 1996). It is therefore already clear that considerable caution must be exercised in interpreting the results of fits to gravitational lens systems.

The approach of modellers has been largely two-pronged. First, general non-parametric methods have been developed (e.g., Saha & Williams 1997). These have proved powerful in exploring the range of degeneracies in the lensing mass that can give rise to a particular image configuration. For example, in the case of PG 1115+080, Saha & Williams present three different models obeying the lens-

ing constraints, but for which the lensing mass distribution resembles a face-on spiral, an edge-on disk or a flattened elliptical galaxy respectively. Second, many simple parametric models have been thoroughly explored, such as those based on elliptically stratified potentials (e.g., Witt 1996; Witt & Mao 1997) or densities (e.g., Kassiola & Kovner 1993; Muñoz, Kochanek & Keeton 2001). The advantage of this is that the models may already incorporate some of the known properties of nearby galaxies. However, this approach may also be dangerous because simple ansatze like elliptical potentials or surface mass densities can introduce unexpected properties. These properties may be so severe that, for example, the flux ratios may not be well fitted and wrong conclusions may be drawn. This can be seen most clearly in the case of elliptical potentials, in which there are strong constraints on the flux ratios (e.g., Witt & Mao 2000; Hunter & Evans 2001).

All this attains added significance in the light of recent claims of evidence for substructure from “anomalous flux ratios” in strong lensing. Mao & Schneider (1998) were the first to point out that substructure may be needed to explain the flux ratios in some cases. The instance that they selected, the quadruplet B 1422+231, has three highly magnified bright images and one much fainter image. Three highly magnified images occur generically near a cusp, and a Taylor expansion gives a universal relationship that the sum of the fluxes of the two outer images should equal the flux of the middle image. This is strongly violated in B 1422+231 leaving substructure on top of the smooth model as the believable culprit. This result is supported by the detailed models of B 1422+231 by Bradac et al. (2002) which find that the discrepancy requires substructure on the mass scale $\sim 10^6 M_\odot$. Very recently, Dalal & Kochanek (2002) looked at seven radio quadruplets and argued that the flux ratios were anomalous by comparison with those expected for simple isothermal lenses with external shear. They claimed that the anomalous flux ratios implied the existence of $\sim 2\%$ of the mass of the lensing galaxy in substructure. Metcalf & Zhao (2002) looked at five optical quadruplets and similarly claimed evidence for anomalous flux ratios on comparison with those expected for simple elliptical power-law potentials with shear. The problem with this procedure is, of course, that anomalous flux ratios may not be the result of substructure at all, but may simply reflect deficiencies in the modelling.

This motivates us to introduce in sections 2 and 3 a new approach for fitting which can incorporate the flux ratios at outset and allows us to introduce an arbitrary number of free parameters. Importantly, all the free parameters enter linearly into the model and so *the lens and flux ratio equations can always be solved by straightforward matrix inversion*. The models are only restricted by the fact that the surface mass density must be positive. This algorithm is used in section 4 to assess the evidence for anomalous flux ratios.

2 SCALE-FREE MODELS

2.1 Potential and Surface Mass Density

Scale-free galaxy models with arbitrary power-law fall-off are widely used in galactic astronomy and dynamics (e.g.,

Toomre 1982; Evans 1994; Evans, Carollo & de Zeeuw 2000). The isophotes of a scale-free galaxy have the same shape at every radius and are completely described by a *shape function* $G(\theta)$, which depends only on the position angle θ with respect to the major axis. In such galaxies, the convergence κ and deflection potential ϕ are proportional to a power of r , namely

$$\kappa = \frac{1}{2}G(\theta)r^{\beta-2}, \quad \phi = r^\beta F(\theta). \quad (1)$$

Here, (r, θ) are familiar polar coordinates in the lens plane. The power is restricted to lie in the range $0 < \beta < 2$ for galaxy models. For $\beta < 0$, the mass at the centre of the galaxy does not converge. For $\beta > 2$, the surface mass density increases with radius, which is unrealistic. The important $\beta = 1$ case corresponds to an everywhere flat rotation curve.

From Poisson’s Law, we have

$$G(\theta) = \beta^2 F(\theta) + F''(\theta). \quad (2)$$

Using the method of variation of the parameters (e.g., Bronstein & Semendyayev 1998, section 3.3.1.3.4; Evans & Witt 2001), we obtain

$$\begin{aligned} F(\theta) = & \frac{\sin(\beta\theta)}{\beta} \int_0^\theta G(\vartheta) \cos(\beta\vartheta) d\vartheta \\ = & \frac{\cos(\beta\theta)}{\beta} \left[\int_{\frac{\pi}{2}}^\theta G(\vartheta) \sin(\beta\vartheta) d\vartheta \right. \\ & \left. - \cot\left(\frac{\pi\beta}{2}\right) \int_0^{\frac{\pi}{2}} G(\vartheta) \cos(\beta\vartheta) d\vartheta \right], \end{aligned} \quad (3)$$

which establishes the relation between the potential and the surface mass density.

The critical curves can be given analytically. Using the determinant of the Jacobian, we obtain

$$\begin{aligned} \det J(r, \theta) = & (\beta - 1)r^{2\beta-4}[\beta FF'' - (\beta - 1)F'^2 + \beta^2 F^2] \\ & - r^{\beta-2}[F'' + \beta^2 F] + 1 = 0. \end{aligned} \quad (4)$$

Setting $\rho = r^{\beta-2}$ yields a quadratic equation in ρ which easily can be solved with a computer. The two roots correspond to the radial and the tangential critical curves respectively. We note that for the flat rotation curve case ($\beta = 1$), the equation for the critical curve becomes linear and thus very simple, as established in Evans & Witt (2001).

2.2 Fourier Expansions

Since $F(\theta)$ and $G(\theta)$ are periodic with period 2π , we can expand them as Fourier series (see e.g. Bronstein & Semendyayev 1998). For convenience, we start with the potential $F(\theta)$ and write

$$F(\theta) = \frac{a_0}{2} + \sum_{k=1}^{\infty} [a_k \cos(k\theta) + b_k \sin(k\theta)]. \quad (5)$$

Using eq.(2), we obtain now for $G(\theta)$

$$G(\theta) = \frac{a_0}{2} + \sum_{k=1}^{\infty} [a_k(\beta^2 - k^2) \cos(k\theta) + b_k(\beta^2 - k^2) \sin(k\theta)]. \quad (6)$$

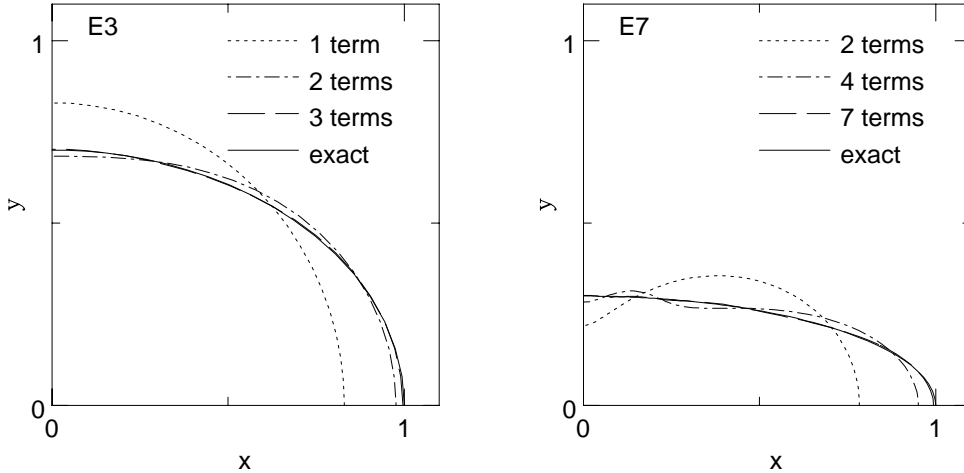


Figure 1. The two plots show truncated Fourier series approximations to the isophotes of an E3 (left panel) and an E7 (right) galaxy with exactly elliptical isophotes. For moderate flattenings such as E3, excellent results are obtained with only the first three non-vanishing terms in the expansion. Even for the most highly flattened configurations such as E7, the approximation becomes very accurate when the first seven non-vanishing terms are included.

This is the Fourier series for $G(\theta)$. Note that the coefficients must obey the condition $G(\theta) \geq 0$ for all θ to obtain a positive surface mass density.

As an example, let us consider the elliptical surface mass density, which has

$$G(\theta) = A(\cos^2 \theta + q^{-2} \sin^2 \theta)^{-1/2}. \quad (7)$$

Since $G(\theta) = G(-\theta)$ is an even function, all b_k must vanish ($b_k = 0$). Since $G(\theta) = G(\pi - \theta)$, all a_k with k equal to an odd integer must also vanish. So, the only terms that remain in the Fourier series are the even integer cosine coefficients (cf. also Appendix A). Figure 1 shows how few terms are really required for accurate approximation. For an E3 galaxy, a Fourier series truncated after the first three non-vanishing terms already gives an excellent approximation to the true isophotes. Even for a highly flattened E7 galaxy, only the first seven non-vanishing terms are needed. This demonstrates that the Fourier expansions can give good results with few terms.

As we show in the next section, the advantage of the Fourier expansion is that it makes it very easy to solve the lens equation. For this reason, we list the Fourier coefficients for the popular elliptic density and potential models with flat rotation curves in Appendix A (although we do not need to use them in this paper).

2.3 The Image Positions and Fluxes

The lens equation relates the position of the source (ξ, η) to the positions of the image (x, y) through the derivative of the lensing potential (e.g., Schneider, Ehlers & Falco 1992)

$$\xi = x - \frac{\partial \phi}{\partial x}, \quad \eta = y - \frac{\partial \phi}{\partial y}. \quad (8)$$

Using polar coordinates in the image plane, the lens equation can be recast as

$$\xi = r \cos \theta - r^{\beta-1} [\beta \cos \theta F(\theta) - \sin \theta F'(\theta)], \quad (9)$$

$$\eta = r \sin \theta - r^{\beta-1} [\beta \sin \theta F(\theta) + \cos \theta F'(\theta)], \quad (10)$$

where we can express $F(\theta)$ and $F'(\theta)$ by Fourier series. Let us assume that we have measured the image positions (r_ℓ, θ_ℓ) (in polar coordinates) of a gravitational lens and inserted them into the lens equation. Immediately, we notice that all unknown quantities (i.e. ξ , η , and all a_i and b_i) enter linearly into the lens equation, except for β .

Let us now add in the constraint that the magnification ratios of the images are equal to the observed values. Suppose that the ratio of the magnification of the ℓ th image to the k th is measured to be $f_{k\ell}$, then

$$f_{k\ell} = \frac{\det J(r_\ell, \theta_\ell)}{\det J(r_k, \theta_k)}, \quad (11)$$

where $\det J$ is given in eq. (4). We observe that the coefficients a_i and b_i enter in simple mixed quadratic form into the equations. However, for the special case of a flat rotation curve ($\beta = 1$), all unknown quantities enter linearly into the equation for the magnification relation.

In other words, *in the astrophysically important flat rotation curve case, the Fourier coefficients describing the lensing galaxy are related to the observables by a simple matrix equation*. This makes the problem of fitting to the lensing observables a straightforward matter of matrix inversion.

3 FITTING GRAVITATIONAL LENSES

3.1 A Singular Value Decomposition Problem

First, we insert the Fourier series of $F(\theta)$ into eqs. (9)-(10) to establish the linear equations for fitting for $\beta = 1$. Intro-

	$-\Delta\alpha$ (in '')	$\Delta\delta$ (in '')	Radio fluxes (in μ Jy)	Mid-infrared flux fractions	H band (in mags)	I band (in mags)
A	0.0	0.0	65.5 ± 8.4	0.27 ± 0.02	14.96 ± 0.06	15.92 ± 0.12
B	0.673 ± 0.003	1.697 ± 0.003	64.2 ± 8.4	0.30 ± 0.02	15.46 ± 0.02	17.21 ± 0.11
C	-0.635 ± 0.003	1.210 ± 0.003	26.5 ± 8.4	0.16 ± 0.02	15.71 ± 0.03	16.77 ± 0.12
D	0.866 ± 0.003	0.528 ± 0.003	59.4 ± 8.4	0.27 ± 0.02	16.00 ± 0.04	17.39 ± 0.04
G	0.075 ± 0.004	0.939 ± 0.003				

Table 1. Observational data on the Einstein Cross. The optical positions are taken from the CASTLES survey, as are the H and I band fluxes. The radio fluxes are provided by Falco et al. (1996). The mid-infrared flux fractions are given in Agol, Jones & Blaes (2000).

Band	ξ	η	a_0	a_2	b_2	a_3	b_3	a_4	b_4	a_5	b_5
Radio	0.0636	-0.0125	1.7767	-0.0419	0.0424	0.0004	-0.0008	0.0002	0.0010	-0.0000	-0.0001
Mid-IR	0.0676	-0.0126	1.7710	-0.0422	0.0414	0.0000	0.0000	0.0000	0.0000	0.0000	0.0000
I	0.0697	-0.0262	1.7655	-0.0353	0.0491	-0.0010	0.0007	-0.0007	-0.0009	0.0014	0.0008
H	0.0700	-0.0196	1.7698	-0.0389	0.0459	-0.0004	0.0005	-0.0000	-0.0004	0.0008	0.0009

Table 2. Coefficients of the solutions for the Einstein Cross. These coefficients correspond to the bold lines in Figure 2, for which the positions and flux ratios are reproduced within the errors.

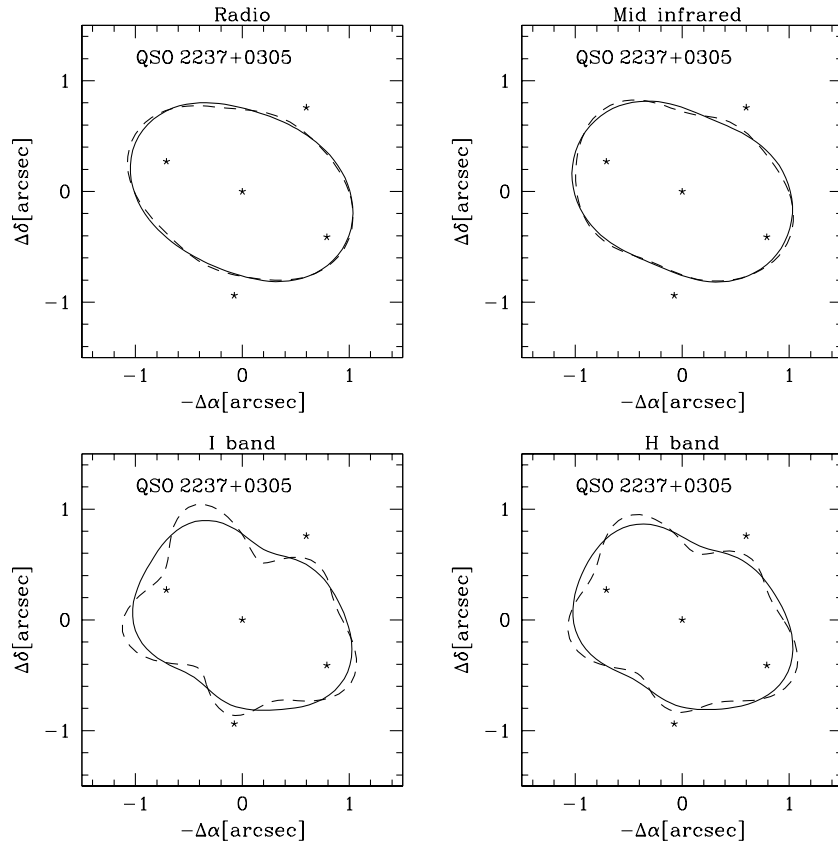


Figure 2. The panels show an equidensity contour (or equivalently, the critical curve) of a lens model for the Einstein Cross that exactly fits the image positions and the flux ratios as a dashed curve. The full curve shows the equidensity contour of a model that fits the data within the uncertainties. Working clockwise from the top left, the panels use the flux ratios in the radio, mid infrared, H band and I band respectively. The locations of the four images and the lensing galaxy are also marked. Even for the most discrepant bands (I and H), the flux ratios are reproduced to within 10 % by the bold curves.

ducing a useful notation, we write for the lens equation

$$\xi(r, \theta) = r \cos \theta - \frac{a_0}{2} \alpha_0(\theta) - \sum_{k=1}^{\infty} a_k \alpha_k(\theta) + b_k \beta_k(\theta), \quad (12)$$

$$\eta(r, \theta) = r \sin \theta - \frac{a_0}{2} \hat{\alpha}_0(\theta) - \sum_{k=1}^{\infty} a_k \hat{\alpha}_k(\theta) + b_k \hat{\beta}_k(\theta), \quad (13)$$

where a_k and b_k are the Fourier coefficients of the unknown function $F(\theta)$, which describes the angular part of the potential. For the coefficients α_k and β_k , we find

$$\begin{aligned} \alpha_k(\theta) &= \cos \theta \cos(k\theta) + k \sin \theta \sin(k\theta), \\ \beta_k(\theta) &= \cos \theta \sin(k\theta) - k \sin \theta \cos(k\theta), \end{aligned} \quad (14)$$

and for $\hat{\alpha}_k$ and $\hat{\beta}_k$, we find

$$\begin{aligned} \hat{\alpha}_k(\theta) &= \sin \theta \cos(k\theta) - k \cos \theta \sin(k\theta), \\ \hat{\beta}_k(\theta) &= \sin \theta \sin(k\theta) + k \cos \theta \cos(k\theta), \end{aligned} \quad (15)$$

for all $k \geq 0$. The lens equations (9)-(10) must hold at the positions of the n images, given in polar coordinates as (r_ℓ, θ_ℓ) with $\ell = 1, \dots, n$. This provides $2n$ constraints on the unknown source position (ξ, η) and the unknown Fourier coefficients.

Now let us consider the magnification of the ℓ th image. For the flat rotation curve case ($\beta = 1$), we obtain

$$\det J = \frac{1}{p_\ell \mu_\ell} = 1 - \frac{G(\theta_\ell)}{r_\ell}, \quad (16)$$

where p_ℓ is the parity of the image ℓ . It is only the flux ratios that can be related to the observational data, not the magnifications themselves. For the flux ratio of image ℓ compared to image k , we obtain

$$f_{k\ell} = \frac{p_k \mu_k}{p_\ell \mu_\ell} = \frac{1 - G(\theta_\ell)/r_\ell}{1 - G(\theta_k)/r_k}. \quad (17)$$

The flux ratio may be *positive* or *negative* depending on the combination of parities of the images. For flux ratios, we always compare to a reference image, which without loss of generality we take as the first image. Clearing the fractions, we can write the equation in a similar form to the lens equation

$$(f_{1\ell} - 1)r_1 r_\ell = \frac{a_0}{2} \gamma_0(\theta_\ell) + \sum_{k=1}^{\infty} a_k \gamma_k(\theta_\ell) + b_k \delta_k(\theta_\ell), \quad (18)$$

with

$$\begin{aligned} \gamma_k(\theta_\ell) &= (1 - k^2)(f_{1\ell} r_\ell \cos(k\theta_1) - r_1 \cos(k\theta_\ell)) \\ \delta_k(\theta_\ell) &= (1 - k^2)(f_{1\ell} r_\ell \sin(k\theta_1) - r_1 \sin(k\theta_\ell)). \end{aligned} \quad (19)$$

This provides a further $n-1$ linear constraints on the unknowns.

Now let us introduce a compact notation to facilitate matters. We set $\alpha_{k\ell} \equiv \alpha_k(\theta_\ell)$, where the first index denotes the Fourier component and the second index the image number. Exactly similar definitions can be made for $\beta_{k\ell}$, $\hat{\alpha}_{k\ell}$, $\hat{\beta}_{k\ell}$, $\gamma_{k\ell}$ and $\delta_{k\ell}$. We are now ready to set up the matrix equation for the fitting to the positions of the images and the flux ratios. Let us write

$$Cx = d \quad (20)$$

where

$$d = (r_\ell \cos \theta_\ell, \dots, r_\ell \sin \theta_\ell, \dots, (f_{1\ell} - 1)r_1 r_\ell, \dots)^T \quad (21)$$

is a vector of $3n-1$ observables. Here, ℓ runs from 1 to n for a lens system with n images. There is always one less equation for the flux constraints than for the image position constraints. The vector

$$x = (\xi, \eta, a_0/2, a_1, a_2, a_3, \dots)^T \quad (22)$$

contains the unknown quantities, namely the source coordinates (ξ, η) , and the Fourier coefficients. There are in principle infinitely many such coefficients, but in practice the Fourier series is usually terminated so that x is a vector of $3n-1$ components as well. Finally, for the matrix C , we obtain

$$C = \begin{pmatrix} 1 & 0 & \alpha_{0\ell} & \alpha_{1\ell} & \beta_{1\ell} & \alpha_{2\ell} & \beta_{2\ell} & \dots \\ \cdot & \dots \\ 0 & 1 & \hat{\alpha}_{0\ell} & \hat{\alpha}_{1\ell} & \hat{\beta}_{1\ell} & \hat{\alpha}_{2\ell} & \hat{\beta}_{2\ell} & \dots \\ \cdot & \dots \\ 0 & 0 & \gamma_{0\ell} & \gamma_{1\ell} & \delta_{1\ell} & \gamma_{2\ell} & \delta_{2\ell} & \dots \\ \cdot & \dots \end{pmatrix} \quad (23)$$

Provided we can measure all n image positions and $n-1$ flux ratios, then C has $3n-1$ rows. The number of columns is in principle arbitrarily large, although in practice it usually makes sense to terminate the Fourier series so that C is a $3n-1 \times 3n-1$ matrix.

As it stands, the matrix C is always singular ($\det C = 0$). There exists a null space for the matrix C , i.e., there exists at least one non-vanishing vector x_0 which satisfies the equation $Cx_0 = 0$. In fact, the matrix C has (at least) a two-dimensional null space. Fortunately, the null subspace can be easily constructed. Since $\alpha_{1\ell} = 1$, $\beta_{1\ell} = 0$, $\hat{\alpha}_{1\ell} = 0$, $\hat{\beta}_{1\ell} = 1$, $\gamma_{1\ell} = 0$ and $\delta_{1\ell} = 0$ for all ℓ , it is easy to verify that the null vector must be of the form $x_0 = \lambda_1 v_1 + \lambda_2 v_2$ with $v_1 = (1, 0, 0, -1, 0, \dots)^T$ and $v_2 = (0, 1, 0, 0, -1, 0, \dots)^T$.

From the physical point of view, the Fourier coefficients a_1 and b_1 simply produce a shift or transformation of the source position (ξ, η) . However, both coefficients do not contribute to the surface mass density for the special case of $\beta = 1$ since $a_1 \cos \theta$ and $b_1 \sin \theta$ are solutions of the homogeneous differential equation $F(\theta) + F''(\theta) = 0$ (cf. eq.(2)). We can excise this degeneracy by simply setting $a_1 = b_1 = 0$, which corresponds to the choice of origin. Now we can just remove the 4th and 5th column of the matrix C and add two higher degree Fourier coefficients to the problem to maintain C as a $3n-1 \times 3n-1$ matrix. In this case, the matrix may be written now as

$$C = \begin{pmatrix} 1 & 0 & \alpha_{01} & \alpha_{21} & \beta_{21} & \alpha_{31} & \beta_{31} & \dots \\ \cdot & \dots \\ 0 & 1 & \hat{\alpha}_{01} & \hat{\alpha}_{21} & \hat{\beta}_{21} & \hat{\alpha}_{31} & \hat{\beta}_{31} & \dots \\ \cdot & \dots \\ 0 & 0 & \gamma_{02} & \gamma_{22} & \delta_{22} & \gamma_{32} & \delta_{32} & \dots \\ \cdot & \dots \end{pmatrix} \quad (24)$$

and the vector of unknowns becomes

$$x = (\xi, \eta, a_0/2, a_2, a_3, b_3, \dots)^T \quad (25)$$

The above matrix is usually non-singular and so a Gauss-Jordan elimination can formally solve the problem. However, it is better to use singular value decomposition to solve for the unknown vector x (cf. Press et al. 1999). In this way, we are always guaranteed to find a numerically stable solution.

Let us remark here that one can add further higher degree Fourier coefficients and then the fitting problem becomes underdetermined. We can obtain a whole space of

models all of which would equally well reproduce the observed data. It is clear – even with the severe restriction that we have made to a scale-free model with a flat rotation curve – that the variety of models that fit the data is extremely large. This cautions us against making rash statements based on goodness-of-fit to a single model.

3.2 Error Propagation

One of the advantages of this method is that the transmission of errors is particularly easy to handle. It is of modest interest to provide a model that fits the observational data exactly, as the uncertainties in the flux ratios are substantial. It is of much greater interest to be able to find a set of models that can reproduce the data within the errors.

Suppose the error in each observable in eq. (21) is σ_i . Then, we rescale so that

$$C_{ij} \rightarrow C_{ij}/\sigma_i, \quad d_i \rightarrow d_i/\sigma_i. \quad (26)$$

The singular value decomposition of the rescaled matrix C is

$$C = U \cdot W \cdot V^T \quad (27)$$

where the $3n-1 \times 3n-1$ matrices U and V are orthonormal, and the matrix W is a diagonal matrix of singular values $(w_1, w_2, \dots, w_{3n-1})$. As usual in a singular value decomposition, any very small singular values are removed (see Press et al. 1989). After deletion, let us suppose that m singular values remain, where $m \leq 3n-1$.

The boundaries of the error ellipsoid in the space of fitted parameters is

$$\Delta = w_1^2 (\mathbf{V}_{(1)} \cdot \delta \mathbf{x})^2 + \dots + w_m^2 (\mathbf{V}_{(m)} \cdot \delta \mathbf{x})^2 \quad (28)$$

Here, \mathbf{V}_m is the m th column of the matrix V , while Δ is chosen such that the probability of a chi-square variable with M degrees of freedom being less than Δ is 0.68. For a one degree of freedom problem of a normally distributed chi-square variable, this error ellipsoid collapses down to the familiar 1σ error bars. For our more general problem, the columns of the orthonormal matrix V define the principal axes of the error ellipsoid in the fitted parameters. The lengths of the axes are inversely proportional to the singular values.

In the flux ratios, almost all the error is of course caused by systematic effects like microlensing or differential extinction or scatter-broadening. Hence, we always assume that the measured flux ratios are in error by 15%. The relative positions of the images with respect to the centre of the lensing galaxy are generally much more accurately known. Nonetheless, the images themselves are not point-like dots but distended regions of emission, while the centre of the lensing galaxy is often poorly known (especially if it is at high redshift). Again, the formal error in the astrometry is therefore much less than the systematic errors in the positions. We typically assume that the measured positions are in error by 5%. A good way to convince oneself that these uncertainties are only too realistic is to look at the discrepancies in the values reported by different sets of observers for the same gravitational lens.

3.3 Position Angle of the Lensing Galaxy

The axes of the local right ascension and declination coordinates may be rotated by an arbitrary angle with respect to the major and minor axes of the lensing galaxy. This is implicitly contained in the derived Fourier coefficients.

We can expand the Fourier series as

$$\begin{aligned} & \sum_{k=1}^{\infty} a_k \cos(k\theta) + b_k \sin(k\theta) \\ &= \sum_{k=1}^{\infty} a_k^R \cos(k\theta + \theta_R) + b_k^R \sin(k\theta + \theta_R), \end{aligned} \quad (29)$$

where θ_R is the rotation angle and a_k^R and b_k^R are the Fourier coefficients in the rotated coordinate system. It is easy to verify that

$$a_k^R = a_k \cos \theta_R + b_k \sin \theta_R \quad b_k^R = -a_k \sin \theta_R + b_k \cos \theta_R. \quad (30)$$

If the lensing galaxy has a major axis, the following condition must be satisfied:

$$G'(\theta_R) \approx 0 \approx G'(\theta_R + 180^\circ). \quad (31)$$

If the lensing galaxy looks regular, it probably has, in addition to a major axis, an approximate reflection symmetry $G(\theta) \approx G(-\theta)$, or equivalently $F(\theta) \approx F(-\theta)$. Therefore, in the rotated system, we expect $b_k^R \approx 0$ for all k . In other words, the rotated system is defined by

$$\sum_{k=1}^n (b_k^R)^2 = \text{minimum.} \quad (32)$$

Solving this equation yields the rotation angle of the major axis of the lensing galaxy

$$\tan(2\theta_R) = 2 \sum_{k=1}^n a_k b_k / \sum_{k=1}^n (a_k^2 - b_k^2). \quad (33)$$

3.4 Mass inside the Einstein Ring

Evans & Witt (2001) showed that the mass inside the Einstein ring must be very close to the mass inside the critical curve for the special case of $\beta = 1$. We therefore can write

$$\begin{aligned} M_E &\approx M_{\text{crit.curve}} = \frac{1}{2\pi} \int_0^{2\pi} G^2(\theta) d\theta \\ &= \frac{a_0^2}{2} + \sum_{i=2}^N (k^2 - 1)^2 (a_k^2 + b_k^2). \end{aligned} \quad (34)$$

To apply this to a real lens, we have to scale the result by the factor $\Sigma_{\text{crit}} D_{\text{d}}^2$ containing the normalized surface mass density which is given by

$$\Sigma_{\text{crit}} = \frac{c^2 D_{\text{s}}}{4\pi G D_{\text{d}} D_{\text{ds}}}. \quad (35)$$

Here, D_{d} , D_{s} and D_{ds} are the distance to the deflector, the distance to the source and the distance from the deflector to the source respectively. Given the redshift of the lens and the source, this (35) enables the projected mass within the Einstein ring to be estimated.

	$-\Delta\alpha$ (in '')	$\Delta\delta$ (in '')	I band (in mags)	H band (in mags)
A1	-1.328 ± 0.004	-2.034 ± 0.004	16.12	15.71 ± 0.03
A2	-1.477 ± 0.004	-1.576 ± 0.003	16.51	16.21 ± 0.04
B	0.341 ± 0.003	-1.961 ± 0.004	18.08	17.70 ± 0.05
C	0	0	17.58	17.23 ± 0.04
G	-0.381 ± 0.003	-1.344 ± 0.003		

Table 3. Observational data on the quadruplet PG 1115+050. The optical positions are taken from the CASTLES survey, as are the H band fluxes. The I band fluxes come from Kristian et al. (1993).

	$-\Delta\alpha$ (in '')	$\Delta\delta$ (in '')	I band ratio	H band (in mags)
A	0	0	1.00	15.83 ± 0.03
B	-0.744 ± 0.003	0.168 ± 0.003	0.90	15.92 ± 0.02
C	0.492 ± 0.003	0.713 ± 0.003	0.76	16.18 ± 0.03
D	-0.354 ± 0.003	1.040 ± 0.003	0.59	16.43 ± 0.03
G	-0.142 ± 0.003	0.561 ± 0.015		

Table 4. Observational data on the quadruplet H 1413+117. The optical positions are taken from the CASTLES survey, as are the H band fluxes. The I band fluxes come from Kayser et al. (1990).

Lens	Band	ξ	η	a_0	a_2	b_2	a_3	b_3	a_4	b_4
PG 1115+050	H	-0.0339	0.1596	2.3363	-0.0577	0.0746	0.0000	0.0000	0.0000	0.0000
PG 1115+050	I	-0.0340	0.1601	2.3359	-0.0576	0.0744	0.0000	0.0000	0.0000	0.0000
H 1413+117	H	-0.0013	-0.0417	1.2192	0.0417	0.0468	0.0000	0.0000	0.0000	0.0000
H 1413+117	I	-0.0013	-0.0418	1.2189	0.0417	0.0469	0.0000	0.0000	0.0000	0.0000

Table 5. Coefficients for the bold curves solutions for PG 1115+050 and H 1413+117 shown in Figure 3.

4 AN APPLICATION: ANOMALOUS FLUX RATIOS

In this section, we consider four of the lens systems for which substructure has been claimed either by Metcalf & Zhao (2002) or by Dalal & Kochanek (2002) or by Chiba (2002).

4.1 Q 2237+030 (The Einstein Cross)

The data on the four images of Q 2237+030 (the Einstein Cross) are listed in Table 1. Much of this comes from the CASTLES survey¹. Q 2237+030 is an unusual because so much more information is available for the lensing galaxy than is customary. In particular, the redshift of the lens is so small ($z = 0.0494$) that the galaxy's light distribution can be measured (e.g., Wyithe et al. 2002). The lens is a face-on barred galaxy (e.g., Schmidt, Webster & Lewis 1998). The optical fluxes are known to be affected by microlensing (Irwin et al. 1989; Wambsganss, Schneider & Paczyński 1990; Witt & Mao 1994). It is sometimes argued that the radio and infrared fluxes are more reliable because the source emitting region is more extended. If this is the case, then gravitational lens models should use the radio and infrared flux ratios in preference to optical. The flux ratios in the

radio were measured by Falco et al. (1996) with a signal-to-noise of $\sim 2 - 4$. The mid-infrared flux ratios have recently become available thanks to Agol, Jones & Blaes (2000). The flux ratios in radio and mid-infrared are in good agreement, but differ from the optical flux ratios.

Figure 2 shows the critical curves for four models of Q 2237+030. From eq. (16), the critical curve is also an equidensity contour when the rotation curve is flat. As the models are scale-free, the equidensity contours retain the same shape independent of position, although the size of course varies. In each case, the dashed curve describes a model that exactly reproduces the image positions and flux ratios. It is found by a solution of the matrix equation (20) using singular value decomposition.

We assume that the measured flux ratios are in error by 15% and that the measured positions are in error by 5%. This is larger than the reported errors, which do not take into account systematic effects. For example, the optical centres of the lensing galaxy reported by Crane et al. (1991), Rix, Schneider & Bahcall (1992) and by the CASTLES survey are discrepant at the level of $\sim 0.02''$, which is a factor of $\gtrsim 5$ times larger than the formal error bars. We follow the effect of uncertainties in the observables by constructing the error ellipsoids (28) in the fitted parameters corresponding to a 68 % confidence limit. (In a problem with one degree of freedom, the chi-square is normally distributed so that

¹ <http://cfa-www.harvard.edu/castles/>

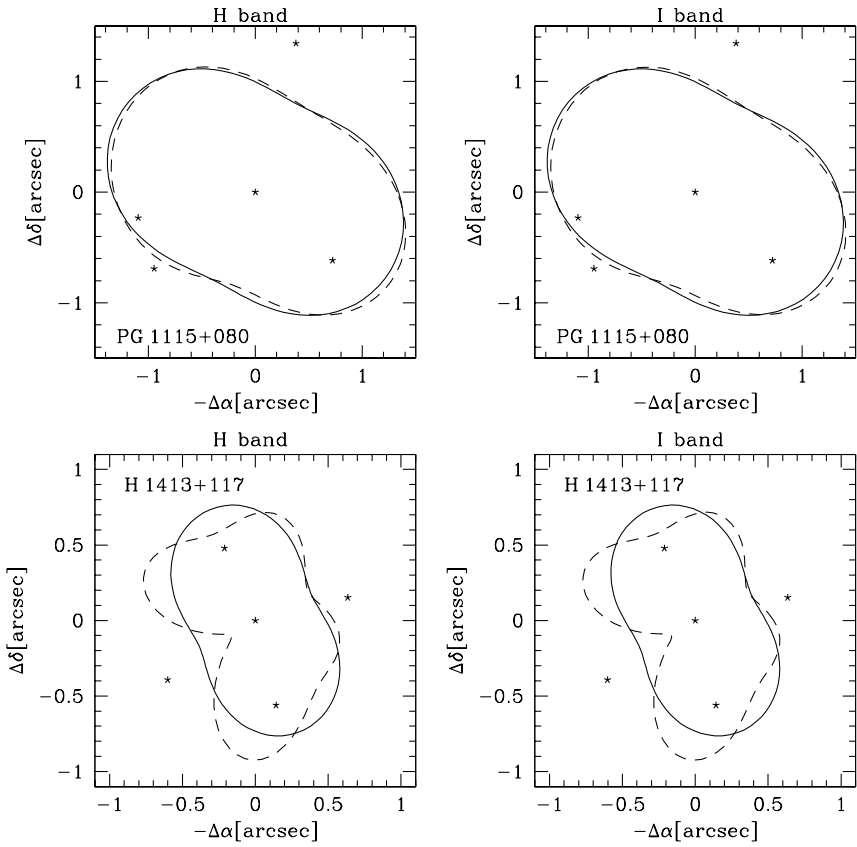


Figure 3. The upper panels refer to PG 1115+050, the lower panels to H 1413+117. The dashed curve shows the exact solution found by singular value decomposition. The full curve shows the equidensity contour of a model that fits the data within the uncertainties. The locations of the four images and the lensing galaxy are also marked. The bold curves for PG 1115+050 reproduce the measured flux ratios to within 6%; for H 1413+117, they reproduce the measured flux ratios to within 11%.

	$-\Delta\alpha$ (in '')	$\Delta\delta$ (in '')	Radio fluxes (in μ Jy)	r band (in mags)	V band (in mags)	H band (in mags)
A	0.0	0.0	216	16.77	16.43 ± 0.11	14.41 ± 0.03
B	0.385 ± 0.003	-0.317 ± 0.003	221	16.45	16.45 ± 0.10	14.29 ± 0.03
C	0.722 ± 0.003	-1.068 ± 0.003	115	17.25	17.09 ± 0.07	14.98 ± 0.03
D	-0.562 ± 0.004	-1.120 ± 0.003	4.5	20.40	20.44 ± 0.06	18.14 ± 0.04
G	-0.375 ± 0.004	-0.973 ± 0.004				

Table 6. Observational data on the quadruplet B 1422+231. The optical positions are taken from the CASTLES survey, as are the H and V band fluxes. The radio fluxes are provided by Patnaik et al. (1992).

this confidence limit corresponds to 1σ uncertainties in the fitted parameter).

The errors define an 11 dimensional error ellipse in the space of fitted parameters, namely the image position (ζ, η) and the Fourier coefficients. Any point within the error ellipse gives a solution which reproduces the observable data within the uncertainty. Hence, any solution in this error ellipse is as good as the exact solution. We do not change $(\zeta, \eta, a_0/2, a_2, b_2)$, although we could if we so wanted. We change the remaining Fourier coefficients by making their absolute value as small as possible, subject to remaining within the error ellipsoid. In other words, out of all the solu-

tions that reproduce the data, we choose the one within the error ellipsoid that most looks like a galaxy, as all Fourier components higher than 2 have been suppressed. The models so produced are shown in bold lines in Figure 2; the details of the solutions are listed in Table 2.

Two points emerge clearly. First, the isodensity contours implied by reproducing the exact radio or infrared fluxes are already in good agreement. The position angle of the lensing galaxy as inferred from eq. (31) is $\sim 55^\circ$ (measured from North through East). This is slightly different from the value of 67° deduced from simple models (e.g., Kochanek 1991). For comparison, Trott & Webster (2002)

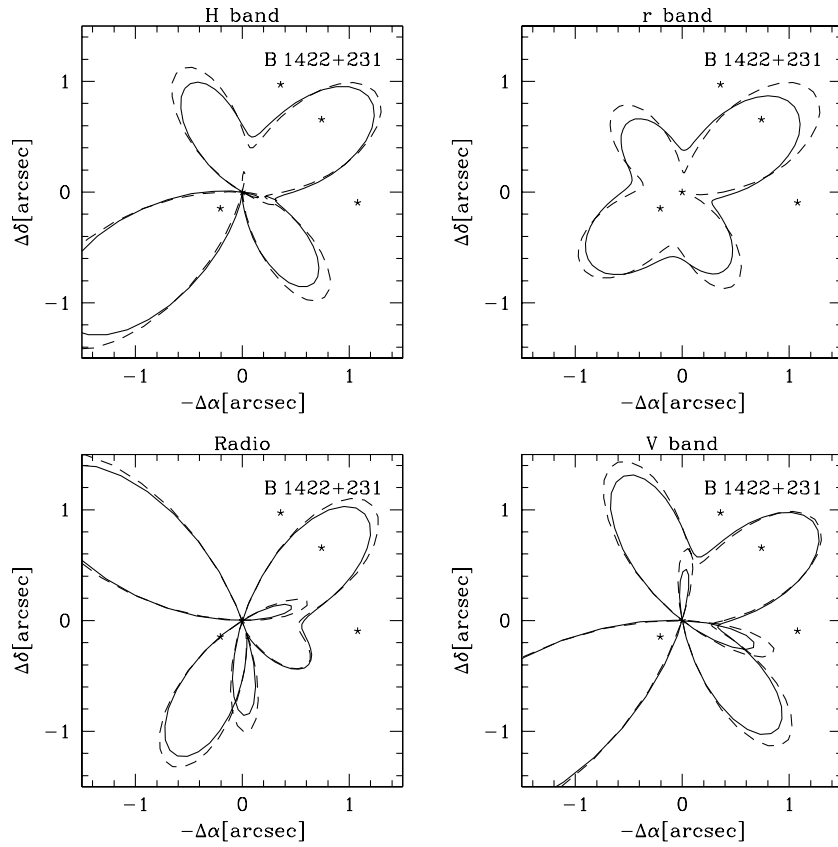


Figure 4. The four panels show equidensity contours for the quadruplet system B 1422+231. Working clockwise from the top left, the panels use the flux ratios in the H band, r band, V band and radio. Any solutions with self-intersecting contours must be discarded as the surface density is not positive definite. This is a lens for which substructure may well be present, as none of our models are at all satisfactory.

report that the position angle of the bar in the lensing galaxy is $\sim 51^\circ$, and that the isophotes twist in the outer parts. Second, the isodensity contours implied by exactly reproducing the I band and the H band optical flux ratios are distorted. However, as the bold line contours in the lower two panels of Figure 2 show, there are much more regular solutions within the error ellipsoid that, moreover, agree with the contours inferred from the radio and infrared data. All this provides strong evidence for the point of view advanced in Agol et al. (2000) that the radio and infrared fluxes are trustworthy and that the optical flux ratios are discrepant because of microlensing. Let us emphasise that all the data are internally consistent once reasonable error bars are placed on the flux ratios and there is no need to invoke substructure to explain the data (c.f. Metcalf & Zhao 2002).

4.2 PG 1115+080 and H 1413+117

We now examine two further lens systems claimed to provide evidence for substructure by either Dalal & Kochanek (2002) or Metcalf & Zhao (2002) or Chiba (2002). The observational data on PG 1115+080 and H 1413+117 are listed in Tables 3 and 4 respectively. There is already evidence that the flux ratios in both these galaxies may come with sub-

stantial uncertainties. For example, Foy, Bonneau & Blazit (1985) found component A2 of PG 1115+080 was brighter than A1 in 1984 March-May, whereas most subsequent investigators have found A2 to be fainter than A1. The conclusion advanced by Christian, Crabtree & Waddell (1987) is that the images in PG 1115+080 are being affected either by microlensing or by time-delayed intrinsic variations in the quasar or both. Evidence for the effects of microlensing in H 1413+117 has been reported by both Kayser et al. (1990) and Angonin et al. (1990) on the grounds on both photometric and spectral variations of image D. Similarly, Chae et al. (2001) detected a dimming of image D by ~ 0.07 magnitudes over a 100 day period in 1999, as well as polarization changes, which they also attributed to microlensing. Radio emission would probably be less affected by microlensing, but both PG 1115+080 and H 1413+117 are radio-quiet and so the optical fluxes have to be used. For both lenses, we implement our fitting procedure to find a solution that exactly reproduces the positions and flux ratios in a given waveband, together with a solution that lies within the errors (whose parameters are listed in Tables 3 and 4.)

In the case of PG 1115+080, the model that reproduces the positions and the flux ratios exactly is shown as a dashed line in the lower panels of Figure 3. This is obtained by

singular value decomposition of the matrix equation (20). The isodensity contours implied by reproducing the exact H band or I band flux ratios are in good agreement. The contours look plausibly like the projected mass distribution of an early-type galaxy. When the errors in the flux ratios are included, a smooth galaxy-like lensing model (shown as a bold line) can satisfactorily reproduce the data without invoking substructure. Despite the claims of Dalal & Kochanek (2002), Metcalf & Zhao (2002) and Chiba (2002), the evidence for substructure in PG 1115+080 is weak.

In the case of H 1413+117, the exact solutions using the H band and I band optical fluxes are denoted by the dashed lines in the lower panels of Figure 3. They are now markedly disturbed from a galaxy-like shape. If the flux ratios were reliable, then substructure might be a possible culprit (although to be certain of this, many more smooth models would have to be examined). However, the bold line, which takes into account likely errors of 5 % in the positions and 15 % in the flux ratios, is a more reasonable contour for a projected galaxy.

For both these cases, the lensing galaxy is at such high redshift that there are few constraints on the lens model. Such information on the lensing galaxy is needed before strong cases for substructure can be built. However, it is clear from the smooth models that we have constructed that there is no really compelling case for substructure in these two lenses at the moment.

4.3 B 1422+231

Patnaik et al. (1992) discovered the gravitational lens B 1422+231 in a radio survey. Table 4 lists some of the available data on the images, largely provided by the CASTLES survey. It was realised by both Kormann, Schneider & Bartelmann (1994) and Hogg & Blandford that it is difficult to reproduce the flux ratios of this lens system with a simple model. Kormann et al. used an elliptical density model with shear, whereas Hogg & Blandford used a mixture of isothermal spheres and point masses.

Figure 4 shows the results of our fitting procedure. Here, we have used the flux ratio data in four bands, but none of the results can be said to be at all satisfactory. The self-intersections in the critical curves when we force reproduction of the fluxes in the radio, the V band and the H band data demonstrate that the mass model contains negative density, and so is completely unphysical. The only physical model is obtained when the r band fluxes are used, but even here the equidensity contours are strongly distorted from that expected in galaxy-like models.

The conclusion to be drawn by the failure of the fitting procedure is that – even taking into account observational uncertainties – this lens system requires additional ingredients. Possibly, as Mao & Schneider (1998) were the first to suggest, substructure may be causing a dramatic effect on the flux ratios. Possibly, as Kundic et al. (1997) suggest, the effects of external shear caused by nearby galaxies and clusters of galaxies may also need to be included in the analysis. What is certainly clear is that no isolated galaxy lens with a flat rotation curve can reproduce the image positions and flux ratios.

5 DISCUSSION

The main aim of this paper is to present a new, simple approach to fitting a model to the data on a gravitational lens. Given the image positions and the flux ratios, a model that exactly fits that data can be constructed by a simple matrix inversion (preferably by singular value decomposition, available in standard numerical libraries). All the fitting parameters enter linearly into the equation. No complicated non-linear χ^2 -fitting needs to be done.

The lensing galaxy is always assumed to be scale-free with a flat rotation curve. There is already a substantial body of evidence from fitting of lenses that early-type galaxies have nearly isothermal profiles (Kochanek 1995; Muñoz et al. 2001; Cohn et al. 2001; Rusin et al. 2002). In particular, the absence of central images strongly constrains the lensing potential of early-type galaxies to be isothermal or steeper (e.g., Rusin & Ma 2001; Evans & Hunter 2002). There is of both stellar dynamical (e.g., Gerhard et al. 2001) and X-ray (Fabbiano 1997) evidence that early-type galaxies have flat rotation curves out to at least 4 effective radii. Hence, our assumption of a flat rotation curve is exactly what the data require.

Unusually, our algorithm allows full flexibility as regards the angular structure of the lensing potential. Earlier fitting procedures have allowed the lensing potential to have different radial structure (for example, different power-law profiles), but usually only simple forms of angular structure (for example, constant external shear). In our models, the radial structure is always fixed at isothermal, but the shape of the density contours is completely arbitrary. The lens model has a flexible number of free parameters, and of course includes isothermal elliptic density and potential models which have a distinguished history in gravitational lens modelling. The fit allows direct deduction of the mass contour of the lensing galaxy. Although we have presented examples based on quadruplet lens systems, the algorithm can be adapted for a two image or a higher image model. A higher image model might be needed, for example, in Q 0957+561, where 10 subimage positions can be detected in the radio band. This lens is heavily distorted by external shear. Such a shear term could be easily added to our algorithm.

The flux ratios may enter directly into the fit depending on whether they are available or trustworthy. We note that flux ratios often do not provide good model constraints. The reason for this is easy to understand. The flux ratios depend on the second derivatives of the lensing potential, whereas time delays and image positions are proportional to the potential and its first derivative respectively. Therefore, flux ratios are particularly sensitive to graininess in the gravitational potential. This often manifests itself as microlensing. The flux ratios are also affected by the uncertain differential extinction corrections that must be applied to each image. Radio and infrared fluxes are generally more reliable than optical. However, scatter-broadening probably affects the radio fluxes in as many as 30% of lenses (Browne, private communication). If flux ratios are incorporated into a fit, it is vital that there is a realistic treatment of the errors. One of the advantages of our fitting algorithm is that the transmission of uncertainties in the observational data to uncertainties in the fitted parameters can be followed in

a straightforward manner and the covariance matrix is directly available.

Our fitting algorithm permits the construction of a whole class of degenerate models all of which can fit the image position and flux ratios exactly. In addition, the models are also degenerate in the time delay since the delay depends only on the distance of the image positions to the centre of the lensing galaxy (cf. Witt, Mao & Keeton 2000). Such degeneracy is easy to understand pictorially. Given a Fermat time delay surface, we need only keep the values, the derivatives and the second derivatives of the surface at the image positions fixed. We then have enormous freedom to move the surface (subject only to the constraints that no additional images are introduced and that no negative mass density is produced).

We have used our new fitting algorithm to examine critically some of the claims made recently for anomalous flux ratios. The procedure used by both Dalal & Kochanek and Metcalf & Zhao was to show that a family of simple models did not reproduce the flux ratios. However, it does not follow from this that substructure is necessary; it may just be that the simple models did not have enough flexibility to provide a good match. For example, of the five lenses studied by Metcalf & Zhao (2002), they themselves concluded that one (MG 0414+0534) could be satisfactorily explained by a smooth model. In this paper, we have demonstrated that the data on three others (PG 1115+080, Q 2237+030, H 1413+117) are consistent with smooth galaxy-like models, especially when a realistic treatment of the errors in the flux ratios is incorporated. This leaves only one candidate from Metcalf & Zhao's sample (B 1422+231) where the case for substructure is strong.

Note that the fraction of mass in substructure expected in galaxy haloes is small ($\lesssim 5\%$) and in general occurs in the outlying portions (e.g., Moore et al. 1999). Substructure evolves as it is subjected to tides, impulsive collisions and dynamical friction. The dynamical friction timescale scales with the square of the galactocentric radius (see e.g., Binney & Tremaine 1987, chap. 7). Within a few tens of kpc, dynamical friction is efficient at dissolving substructure. So, on dynamical grounds, very little substructure ($\lesssim 1\%$) lies projected within the Einstein radius in strong lenses. In other words, to be consistent with cold dark matter theories, substructure can affect the flux ratios of only a very small number of the quadruplets. From our modelling, we tend to agree that the candidate B 1422+231 originally pointed out by Mao & Schneider (1998) is strong. Very recently, using a novel application of the cusp relation, Keeton, Gaudi & Petters (2002) have argued that B 2045+265 and RX J 0911+0551 may be two further good candidates. This method promises to be a more reliable way to identify candidates for substructure than methods based on poor fits to simple models. Certainly, the numbers of strong lenses for which substructure is currently being claimed in the literature are so large that this is in contradiction with cold dark matter theories, not in agreement!

ACKNOWLEDGMENTS

We acknowledge with gratitude the remarkable service provided to the community by the CASTLES website (C.S.

Kochanek, E.E. Falco, C. Impey, J. Lehar, B. McLeod, H.-W. Rix). NWE thanks the Royal Society for financial support and HJW thanks the sub-Department of Theoretical Physics, Oxford for their hospitality during working visits. NWE acknowledges Ian Browne, Leon Koopmans and Jerry Ostriker for a number of interesting discussions. Shude Mao is thanked for a helpful reading of the draft manuscript.

REFERENCES

Agol E., Jones, B., Blaes O. 2000, *ApJ*, 545, 657
 Angonin M.-C., Vanderriest C., Remy M., Surdej J. 1990, *A&A*, 233, L5
 Binney J., Tremaine S. 1987, *Galactic Dynamics*, Princeton University Press
 Bradač M., Schneider P., Steinmetz M., Lombardi M., King L.J., Porcas R. 2002, *A&A*, 388, 373
 Bronshtein I.N., Semendyayev K.A., 1998, *Handbook of Mathematics* (Springer-Verlag, New York)
 Chae K., Turnshek D.A., Schulte-Ladbeck R.E., Rao S.M., Lupie, O.L. 2001, *ApJ*, 561, 653
 Cohn J.D. et al, 2001, *ApJ*, 554, 1216
 Chiba M. 2002, *ApJ*, 565, 17
 Christian C.A., Crabtree D., Waddell P. 1987, *ApJ*, 312, 45
 Crane P. et al. 1991, *ApJ*, 369, L59
 Dalal N., Kochanek C.S. 2002, *ApJ*, 572, 25
 Evans N.W. 1994, *MNRAS*, 267, 333
 Evans N.W., Carollo M., de Zeeuw P.T. 2000, *MNRAS*, 318, 1131
 Evans N.W., Hunter C. 2002, *ApJ*, 575, 68
 Evans N.W., Witt, H.J. 2001, *MNRAS*, 327, 1260
 Fabbiano G. 1989, *ARAA*, 27, 87
 Falco E.E., et al. 1996, *AJ*, 112, 897
 Falco E.E., et al.. 1999, *ApJ*, 523, 617
 Foy R., Bonneau D., Blazit A. 1985, *A&A*, 149, L13
 Gerhard O.E., Kronawitter A., Saglia R.P., Bender R. 2001, *AJ*, 121, 1936
 Hogg D.W., Blandford R.D. 1994, *MNRAS*, 268, 889
 Hunter C., Evans N.W. 2001, *ApJ*, 554, 1227
 Irwin M.J., Webster R.L., Hewett P.C., Corrigan R.T., Jendrzejewski R.I. 1989, *AJ*, 98, 1989
 Jones D.L., et al. 1996, *ApJ*, 470, 23
 Kassiola A., Kovner I. 1993, *ApJ*, 417, 450
 Kayser R., Surdej J., Condon J.J., Kellermann K.I., Magain P., Remy M., Smette A. 1990, *ApJ*, 364, 15
 Keeton C., Gaudi B.S., Petters A.O. 2002, *ApJ*, submitted (astro-ph/0210318)
 Kochanek C.S. 1991, *ApJ*, 373, 354
 Kochanek C.S. 1995, *ApJ*, 445, 559
 Kristian J. et al. 1993, *AJ*, 106, 1330
 Koopmans L.V.E., de Bruyn A.G. 2000, *A&A*, 358, 793
 Kormann R., Schneider P., Bartelmann M. 1994, *A&A*, 286, 357
 Kundic T., Hogg D.W., Blandford R.D., Cohen J.G., Lubin L.M., Larkin J.E. 1997, *AJ*, 114, 2276
 Mao S., Schneider P. 1998, *MNRAS*, 295, 587
 Metcalf R.B., Zhao H.S. 2002, *ApJ*, 567, L5
 Moore B., Ghigna S., Governato F., Lake G., Quinn T., Stadel J., Tozzi P. 1999, *ApJ*, 524, L19

Muñoz J.A., Kochanek C.S., Keeton C.R. 2001, *ApJ*, 558, 657
 Patnaik A.R., Browne I.W.A., Walsh D., Chaffee F.H., Foltz C.B. 1992, *MNRAS*, 259, 1P
 Press W.H., Flannery B.P., Teukolsky S.A., Vetterling W.T. 1999, *Numerical Recipes*, Cambridge University Press, Cambridge
 Rix H.-W., Schneider D.P., Bahcall J.N. 1992, *AJ*, 104, 959
 Rusin D., Ma C.-P. 2001, *ApJ*, 549, L33
 Rusin D. et al. 2002, *MNRAS*, 330, 205
 Saha P., Williams L.L.R. 1997, *MNRAS*, 292, 148
 Schmidt R., Webster R.L., Lewis G.F. 1998, *MNRAS*, 295, 488
 Schneider P., Ehlers J., Falco E.E., 1992, *Gravitational Lenses* (Springer-Verlag, New York)
 Toomre A., 1982, *ApJ*, 259, 535
 Wambsganss J., Schneider P., Paczynski B. 1990, *ApJ*, 358, L33
 Witt H.J., Mao S. 1994, *ApJ*, 429, 66
 Witt H.J. 1996, *ApJ*, 472, L1
 Witt H.J., Mao S. 1997, *MNRAS*, 291, 211
 Witt H.J., Mao S. 2000, *MNRAS*, 311, 689
 Wyithe J.S.B., Agol E., Turner E.L., Schmidt R.W. 2002, *MNRAS*, 330, 575

APPENDIX A: FOURIER COEFFICIENTS OF ELLIPTICAL DISTRIBUTIONS

Let us consider the Fourier expansion of the elliptical distribution

$$F(\theta) = (\cos^2 \theta + q^{-2} \sin^2 \theta)^{-1/2}. \quad (\text{A1})$$

The Fourier coefficients are

$$a_k = \frac{1}{\pi} \int_0^{2\pi} F(\theta) \cos(k\theta) d\theta \quad (\text{A2})$$

$$b_k = \frac{1}{\pi} \int_0^{2\pi} F(\theta) \sin(k\theta) d\theta. \quad (\text{A3})$$

However, the only non-vanishing Fourier coefficients are a_{2n} where n is an integer. The lowest-order terms are

$$\begin{aligned} a_0 &= \frac{4}{\pi} K \\ a_2 &= \frac{8}{\pi(1-q^2)} [(1+q^2)K - 2q^2 E] \\ a_4 &= \frac{4}{3\pi(1-q^2)^2} [(3q^2+1)(q^2+3)K - 8q^2(1+q^2)E] \\ a_6 &= \frac{4}{15\pi(1-q^2)^3} [(1+q^2)(15+98q^2+15q^4)K - 2q^2(23+82q^2+23q^4)E] \\ a_8 &= \frac{4}{105\pi(1-q^2)^4} [-32q^2(1+q^2)(11+74q^2+11q^4)E + (105+1436q^3+3062q^4+1436q^6+105q^8)K], \end{aligned} \quad (\text{A4})$$

where K and E denote the following integrals

$$\begin{aligned} K &= \int_0^{\pi/2} \frac{d\vartheta}{(1 - (1 - q^{-2}) \sin^2 \vartheta)^{1/2}} \\ E &= \int_0^{\pi/2} d\vartheta (1 - (1 - q^{-2}) \sin^2 \vartheta)^{1/2}. \end{aligned} \quad (\text{A5})$$

For elliptical density models, this gives the Fourier series for the shape function $F(\theta)$. Note that the expressions become more and more cumbersome with increasing order. However, the Fourier series converges (numerically) extremely rapidly.

For elliptical density models, exactly the same coefficients hold good but for the Fourier expansion for $G(\theta)$, the angular function in the density. Of course, the Fourier coefficients of $G(\theta)$ are directly related to the Fourier coefficients of the potential contour $F(\theta)$ via eqs. (5) and (6).